

Article

Photochemical Bubble Generation from Polymer Films: Dependence on Molecular Structure and Application for Ultrasound Imaging

Pranaya P. Ghate¹, Christopher Gatpandan², Mohammed N. Almtiri³,
Yahya J. Almualllem³, Rabih O. Al-Kaysi³, and Christopher J. Bardeen^{4,*}

¹ Department of Chemical and Environmental Engineering, University of California, Riverside, CA 92521, USA

² School of Medicine Center for Simulated Patient Care (CSPC), University of California, Riverside, CA 92521, USA

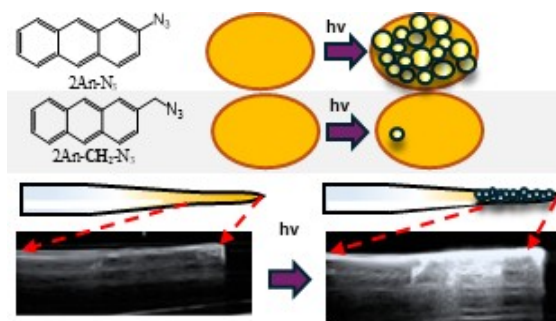
³ College of Science and Health Professions-3124, King Saud bin Abdulaziz University for Health Sciences, and King Abdullah International Medical Research Center (Nanomedicine), Ministry of National Guard Health Affairs, Riyadh 11426, Kingdom of Saudi Arabia

⁴ Department of Chemistry, University of California, Riverside, CA 92521, USA

* Correspondence: christopher.bardeen@ucr.edu

Received: 30 May 2025; Revised: 18 June 2025; Accepted: 20 June 2025; Published: 27 June 2025

Abstract: Photochemical generation of N₂ gas by aromatic azide derivatives dissolved in transparent polymers provides a way to generate bubbles without direct heating. In this work, it is shown that molecules 2-azidoanthracene (2AN-N₃), 2-(azidomethyl)anthracene (2AN-CH₂-N₃), 1-azidopyrene (N₃-PY), and 1-(azidomethyl)pyrene (N₃-CH₂-PY) are all capable of generating stable surface layers of N₂ bubble after exposure to 365 nm light. Bubble formation is modeled as a multistep kinetic process that involves molecular photolysis, gas transport through the polymer, and bubble nucleation in water. Direct conjugation of the azide substituent to the aromatic core leads to more rapid photolysis and facile bubble formation, but even azides with relatively slow reaction rates can generate dense bubble layers if high light intensities are used. Rapid transport of the photogenerated N₂ gas through the polymer appears to be general, with poly(methyl methacrylate), polystyrene and polycarbonate all supporting robust bubble growth. The photoinduced bubble layer was shown to significantly enhance the visibility of a coated glass pipette when imaged by an ultrasound instrument. The ability to prepare polymer coatings that undergo photochemical gas evolution provides a new functionality that may be useful in medical imaging applications.



Keywords: polymers; azide; bubble generation; ultrasound imaging; photolysis

1. Introduction

Stimuli-responsive polymer materials have potential applications in a wide variety of areas, including actuation, sensing, and drug delivery [1–3]. The stimulus can take many forms, including changes in temperature, pH, or humidity. Light is a particularly attractive stimulus because it does not require physical contact with the material or changing the chemical environment. The response can also take many forms and usually involves a change in physical properties like size, optical transmission, or surface morphology. In particular, the initiation of a phase change can have dramatic effects. For example, the generation of a gas from a liquid or solid leads to bubble formation that dramatically modifies material properties like fluid drag [4,5], light transmission [6,7], acoustic wave propagation [8–12], force transmission [13], and heat transport [14]. Photogenerated bubbles are often transient, however, because they are composed of vaporized liquid, usually water [15–19]. Such bubbles are unstable due to recondensation of the vapor after the heat source is removed [20]. Azide photolysis in crystals [21] and polymer hosts [22] provides a photochemical route to stable bubbles composed of N₂ gas. In the polymer system, the N₂ gas rapidly migrates to the surface and nucleates into a dense layer of bubbles that can survive for days under water. These bubbles could be patterned across the surface by controlling the spatial distribution of the photolysis light, and



Copyright: © 2025 by the authors. This is an open access article under the terms and conditions of the Creative Commons Attribution (CC BY) license (<https://creativecommons.org/licenses/by/4.0/>).

Publisher's Note: Scilight stays neutral with regard to jurisdictional claims in published maps and institutional affiliations.

they adhered to the polymer film with sufficient strength to modify its buoyancy. For example, exposure to 365 nm light could induce a submerged polymethyl(methacrylate) (PMMA) film to float to the water surface.

The experimental demonstration of photochemical bubble evolution validated the general concept but left open some questions and challenges. The first question concerns whether the photochemical bubble strategy can be generalized to other azide derivatives and polymer systems. To address this question, we must gain a better understanding of how bubble evolution depends on parameters like photochemical reaction rate, light intensity, and polymer matrix. The second question is whether there exists a practical application for this phenomenon. While buoyancy changes are good for demonstration purposes, it would be more compelling to identify an existing technology and show how it could directly benefit from the ability to generate stable bubble layers after exposure to light.

In this paper, we extend our earlier studies on bubble formation by 2-azidoanthracene ($2N_3$ -AN) dissolved in PMMA to new azide derivatives 2-(azidomethyl)anthracene ($2N_3$ -CH₂-AN), 1-azidopyrene (N_3 -PY), and 1-(azidomethyl)pyrene (N_3 -CH₂-PY) as well as additional polymer systems. We examine the dependence of the azide photodecomposition rate on azide structure in both dilute liquid solution and in solid polymers. We find that direct conjugation of the azide substituent to the aromatic core leads to more rapid photolysis and more facile bubble formation, but even azides with relatively slow reaction rates can generate dense bubble layers if high light intensities are used. Bubble formation can be modeled as a multistep process whose overall rate depends on sequential steps, including molecular photolysis, gas transport through the polymer, and bubble nucleation in water. Rapid transport of the photogenerated N₂ gas through the polymer appears to be a general phenomenon, and other transparent polymers including polystyrene and polycarbonate also support robust bubble growth. Lastly, we demonstrate that a photogenerated bubble layer can dramatically enhance contrast in ultrasound imaging, suggesting that this phenomenon could be useful for medical imaging. The ability to prepare polymer coatings that are photochemically active provides a way to create new types of in situ functionality for devices that operate in challenging environments, like underwater or in biological media.

2. Experimental

2.1. Sample Preparation

The synthesis and characterization of $2N_3$ -AN has been reported previously [22,23]. The synthesis and characterization of $2N_3$ -CH₂-AN, N_3 -PY, and N_3 -CH₂-PY are described in the Supplementary Information. To make polymer films, the azides were dissolved in HPLC-grade chloroform (Fisher Scientific, USA) under low-light conditions and mixed with a solution of poly(methyl methacrylate) (PMMA, Sigma-Aldrich, USA, average molecular weight ~120,000) in CHCl₃. Polystyrene from Sigma-Aldrich (average Mw 280,000) and polycarbonate resin from Acros Organics, USA (average MW 45000) were also used to make films.

Bubble nucleation from the polymer–water interface is strongly influenced by the underlying surface topography. Microscale roughness has previously been shown to facilitate heterogeneous gas nucleation into bubbles by lowering the free energy barrier for phase separation [22,24,25]. To ensure reproducible bubble growth conditions across all samples, polymer films were cast on top of silica-blasted glass slides with a measured RMS roughness of 22 ± 4 μm. This roughened glass acted as a template to ensure uniform roughness for all polymer films. The azide/polymer solution was deposited onto the rough glass surface inside a 1 in. diameter glass cylinder to limit spreading and ensure consistent film diameter and thickness. After enough chloroform had evaporated to make the mixture highly viscous, the glass cylinder was removed, and the films were kept over countertop to dry overnight. After drying, the films were peeled off the roughened glass template to create free-standing polymer samples. The film thicknesses were measured to be 150 ± 25 μm using a Mitutoyo 543–793–10 ID-S112TX Digimatic Indicator (Japan).

2.2. Microscopy

To image bubble formation, the azide/PMMA film was suspended in a water-filled Petri dish with the textured side facing down. The sample was imaged using a stereo microscope model IX50-S8F2 (Olympus Optical Co. Ltd, Japan) with a 4.5× objective and exposed to light from a AloneFire SV-13 UV flashlight (USA) at 365 nm. The light intensity was attenuated with glass neutral density filters (ThorLabs USA) and measured using an Ophir Vega power meter (USA). The light irradiation area was 4.91 cm², and a 0.015 cm² area was imaged using an AmScope MU1000 digital camera (USA). To calculate bubble volume per unit area, frames were extracted from videos at specific time points. Two-dimensional images were analyzed to measure bubble diameters d using the Microsoft Paint application (Paint Windows 11.2503.381.0) to document pixel counts, which were

converted to microns. Individual bubble volumes were calculated with the formula $V = \frac{1}{6}\pi d^3$ and summed up, then divided by the imaged area to obtain the areal volume of N₂ gas.

2.3. Spectroscopy

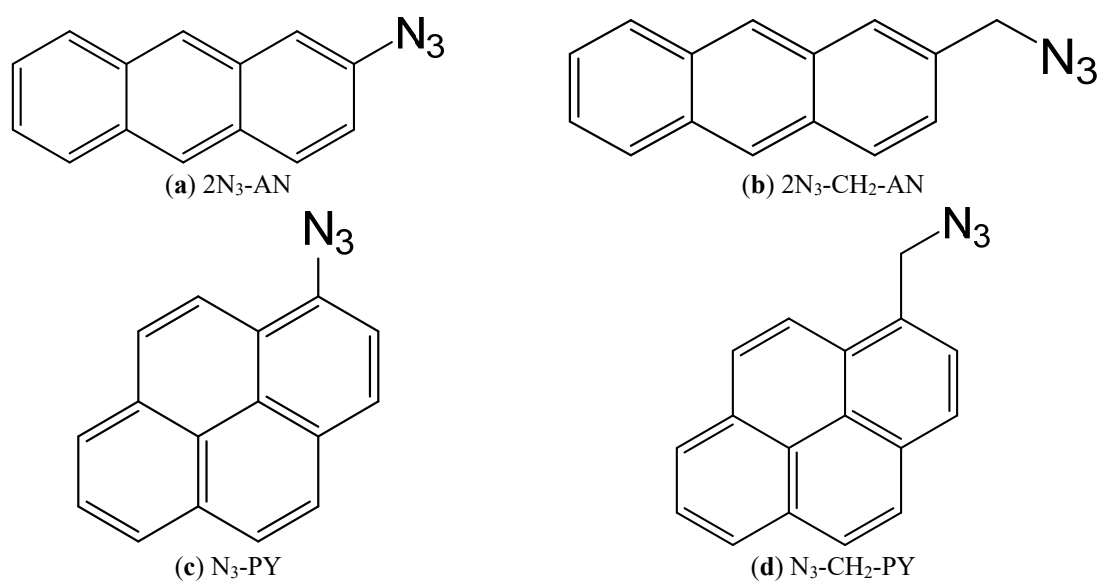
Spectroscopic measurements were carried out using a quartz cell with a path length of 1 cm. The steady state UV-vis absorption was measured using a Varian CARY-60 spectrometer (Agilent Technologies, USA). To monitor the reaction's progress, the azide samples' absorption spectra were collected at 1-s intervals while exposed to 365 nm light from an AloneFire SV-13 UV light source (China). The 365 nm light intensity was controlled by translating the sample with respect to the diverging beam. The reaction rates for all molecules were determined using global fitting [26] implemented using Origin software (OriginLab, USA, academic version 2017). This analysis utilized a single exponential rate time constant to simultaneously fit the time dependent changes for at least 50 wavelengths across the absorption spectrum.

2.4. Ultrasound Measurement

A 2 mm diameter glass pipette was dipped into the azide/PMMA solution and allowed to dry in air. The coated pipette was suspended in a clear acrylic jar filled with water. Ultrasound imaging was performed using a TE7 Max/Diagnostic Ultrasound System (Shenzhen Mindray Bio-Medical Electronics Co., Ltd, Shenzhen, China) with a L14-6s linear array transducer and scanned in B mode. Aquasonic 100 Ultrasound Gel was applied to the interface of the probe and jar to improve acoustic coupling.

3. Results and Discussion

The four molecules shown in Scheme 1 were synthesized using standard methods as detailed in the Supplementary Information (Supplementary Figures S1–S14). The effect of the azide group on the molecular excited states depends on how it is attached to the aromatic core. Figure 1a compares the absorption spectra of unsubstituted anthracene with that of 2N₃-AN and 2N₃-CH₂-AN, while Figure 1b makes the same comparison for the pyrene azides. For both anthracene and pyrene cores, direct attachment of the N₃ group resulted in a large redshift (~25 nm) and reshaping of the absorption spectrum. However, if a methylene group was inserted between the N₃ and the aromatic core, then the original core absorption was largely preserved, albeit with a roughly 10 nm redshift in the case of N₃-CH₂-PY. For both 2N₃-AN and N₃-PY, direct attachment of the N₃ to the conjugated ring likely creates new charge-transfer character the excited state due to the electron-withdrawing azide group. Similar effects have been observed for other aromatic azides [23,27,28].



Scheme 1. The molecular structure of four molecules studied in this paper (a) 2-azidoanthracene 2N₃-AN, (b) 2-(azidomethyl)anthracene 2N₃-CH₂-AN, (c) 1-azidopyrene N₃-PY, and (d) 1-(azidomethyl)pyrene N₃-CH₂-PY.

All the azide derivatives in Scheme 1 undergo photoinduced decomposition to the corresponding nitrene when exposed to ultraviolet (UV) light. Subsequent reactions can lead to formation of nitro groups and other products [22,29,30], but those are not the focus of this paper. The pronounced absorption changes provide a

convenient way to monitor the disappearance of the parent azide. Figure 2 shows a series of UV-Vis spectra taken during photolysis of N₃-PY and 2N₃-CH₂-AN in CHCl₃ solution. Both samples show a well-defined spectral evolution with clear isosbestic points, indicating a single-step transformation to a photoproduct that absorbs across the visible region. Visually, the samples turn from light yellow to brown under light exposure. The other derivatives exhibited similar spectral changes (Supplementary Figure S15). Table 1 provides the measured reaction rates for 365 nm excitation for all four azides in CHCl₃. Since these sample had a relatively low absorbance at 365 nm, we can make the assumption that the intensity variation across the sample is negligible. Under the assumption of constant 365 nm light intensity, dividing the observed reaction rate by the absorption coefficient allows us to estimate relative quantum yields for the azide photolysis. These yields are also given in Table 1, with the highest relative yield (N₃-PY) normalized to 1.0. It is apparent that direct conjugation of the N₃ group to the aromatic core results in a noticeable enhancement in the photolysis quantum yield, especially for pyrene.

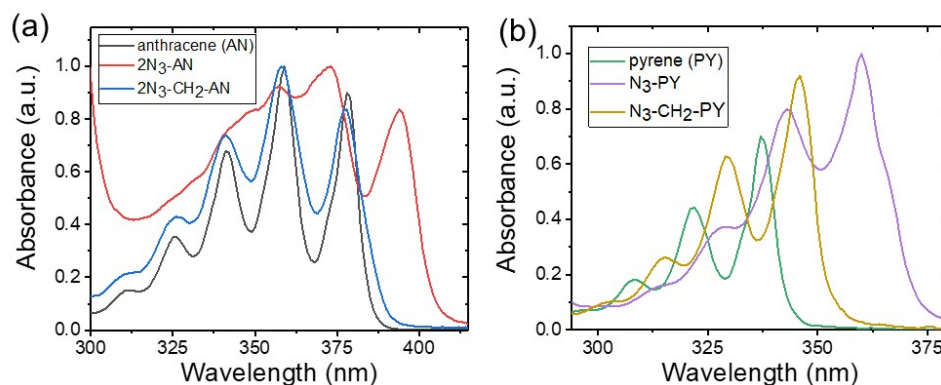


Figure 1. (a) Absorption spectra of anthracene AN (black), 2-azidoanthracene 2N₃-AN (red) and 2-(azidomethyl)anthracene 2N₃-CH₂-AN (blue). (b) Absorption spectra of pyrene PY (green), 1-azidopyrene N₃-PY (purple) and 1-(azidomethyl)pyrene N₃-CH₂-PY (yellow). For both pyrene and anthracene, direct conjugation of the N₃ group leads to a red-shift of the absorption peak.

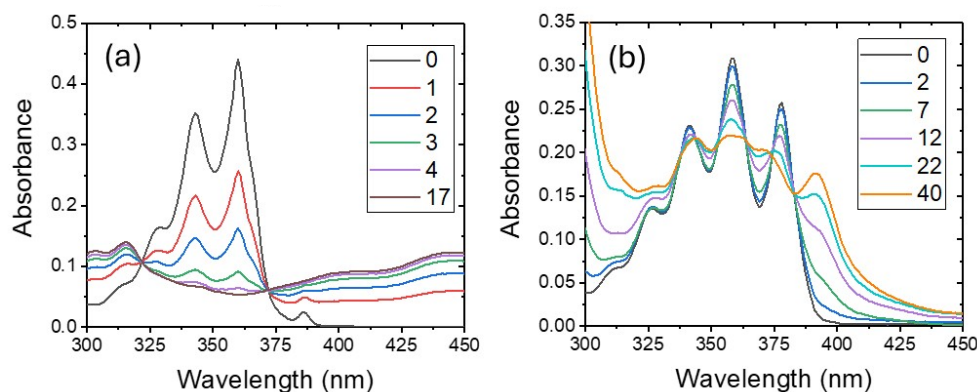


Figure 2. Absorption spectra of (a) N₃-PY and (b) 2N₃-CH₂-AN during irradiation with 365 nm (5 mW/cm²) recorded in chloroform solution. The different color curves show the spectral changes at the time points given in the legend (units of s).

Table 1. Measured reaction rates and relative quantum yields for 365 nm excitation in dilute CHCl₃ solution. Also given are the reaction rates for highly absorbing PMMA films.

Molecule	Rate (s ⁻¹) in Solution	Normalized Relative Quantum Yield	Rate (s ⁻¹) in Film
2N ₃ -AN	0.142	0.9	0.143
2N ₃ -CH ₂ -AN	0.068	0.6	0.002
N ₃ -PY	0.648	1	0.111
N ₃ -CH ₂ -PY	0.035	0.02	0.005

We were unable to find a systematic study in the literature of how azide connectivity affects its photoreactivity. Although it was originally proposed that the N₂ dissociation proceeds thermally through a

vibrationally hot ground state [31], most researchers now believe that it proceeds along a dissociative excited state [32,33]. In either case, dissociation would be expected to be more efficient when the N_3 is directly bound to the core. The intervening CH_2 group would inhibit both electronic coupling and vibrational energy transfer, although the flexibility of the linker may allow the N_3 group to have a closer approach to the core that partially compensates for the extra distance. The results in Table 1 are at least qualitatively consistent with this reasoning. The important conclusion from the solution data is that the set of molecules in Scheme 1 provides a way to vary azide reactivity and see whether it affects bubble formation.

In concentrated azide/PMMA films, the photolysis reaction showed changes in the absorption spectrum similar to those observed in solution, but in some cases without clear isosbestic points. Figure 3 shows the absorption spectra at various points during the photolysis of N_3 -PY and $2N_3$ - CH_2 -AN in PMMA. Unfortunately, these films were too optically dense to make the assumption of constant intensity, which prevented estimation of relative quantum yields. However, there was an even greater variation in the reaction rates in PMMA than in solution, probably due to absorption shifts and the more rigid polymer environment.

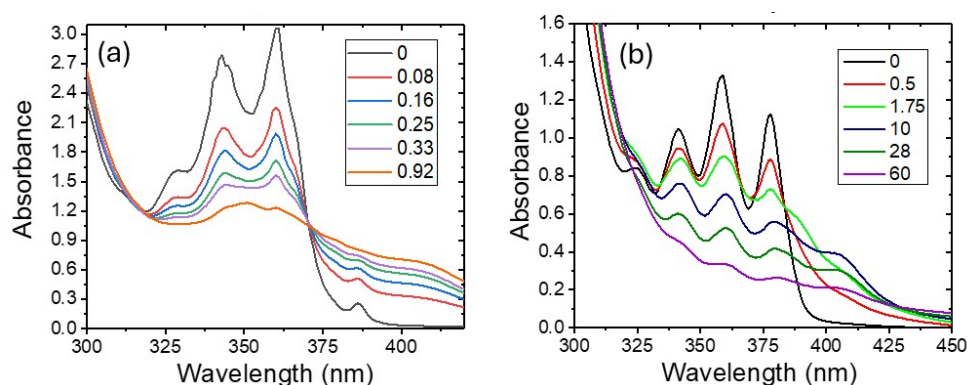


Figure 3. Absorption spectra of (a) N_3 -PY and (b) $2N_3$ - CH_2 -AN during irradiation with 365 nm (9 mW/cm^2) recorded in solid PMMA films with starting concentrations of 0.1 M. The different color curves show the spectral changes at the time points given in the legend (units of min). The much slower decay in the PMMA films is due to the much higher starting absorption values.

We expected the different photochemical reaction rates to impact the bubble formation rate for the azide/PMMA films. To investigate this, we measured the time-dependent volume of bubbles $\bar{V}_{bub}(t)$ produced at the surface by using microscopy analysis. Representative images of bubble formation are shown in Figure 4a–e for the azides in PMMA under 365 nm illumination at 10 mW/cm^2 , along with plots of the growth of the total areal volume of the bubbles, \bar{V}_{bub} . As in our previous paper, the $\bar{V}_{bub}(t)$ curves could be fit to an exponential of the form $\bar{V}_{bub}(t) = \bar{V}_\infty(1 - e^{-k_{bub}t})$. Surprisingly, we found that the k_{bub} rates for the different azides were within 30% of each other (Table 2). But as the intensity was lowered, the bubble forming ability of the different films diverged, until at 0.180 mW/cm^2 the $2N_3$ - CH_2 -AN and N_3 - CH_2 -PY films barely showed any bubble formation at all (Figure 4f–j). At this intensity, the growth for $2N_3$ -AN and N_3 -PY films showed clear induction periods, with the first bubbles only appearing after 60 s of irradiation. These low intensity $\bar{V}_{bub}(t)$ curves could not be fit using the simple exponential growth function.

Table 2. Total areal volume of the bubbles, \bar{V}_{bub} and bubble growth rate constant k_{bub} for all azide molecules at 10 mW/cm^2 and 365 nm irradiation for 0.1 M azide concentration in PMMA films.

Molecule	\bar{V}_{bub} (μm)	k_{bub} (s^{-1})
$2N_3$ -AN	85.92	5.13×10^{-3}
$2N_3$ - CH_2 -AN	47.25	4.65×10^{-3}
N_3 -PY	60.01	6.65×10^{-3}
N_3 - CH_2 -PY	49.40	5.11×10^{-3}

Bubble formation involves several intermediate steps, including N_2 production, diffusion to the polymer-water interface, and finally bubble nucleation, so it is not obvious that this process can be described by a single first-order kinetic process. To analyze the bubble growth dynamics as a multi-step process, we used the kinetic model outlined in Figure 5. The assumption that all processes, including N_2 transport to the surface and bubble nucleation, obey first-order rate laws is clearly a simplification. In particular, bubble nucleation only starts after a threshold density of N_2 molecules has been achieved [34], and a first-order kinetic model will not be able to capture

this behavior. Nevertheless, this model allows us to understand some qualitative features of the data. The coupled rate equations are

$$\frac{\partial C_{azide}}{\partial t} = -k_{photo}C_{azide} \quad (1a)$$

$$\frac{\partial C_{N_2}^{in}}{\partial t} = -k_{esc}C_{N_2}^{in} + k_{photo}C_{azide} \quad (1b)$$

$$\frac{\partial C_{N_2}^{out}}{\partial t} = -k_{bub}C_{N_2}^{out} + k_{esc}C_{N_2}^{in} \quad (1c)$$

$$\frac{\partial \bar{V}_{bub}}{\partial t} = (k_{bub} - k_{diff})C_{N_2}^{out} \quad (1d)$$

C_{azide} , $C_{N_2}^{in}$, $C_{N_2}^{out}$, and V_{bub} are the azide concentration, the concentration of N_2 inside the polymer, the N_2 concentration outside the polymer near the surface, and the areal bubble volume, respectively. The rate of photolysis is k_{photo} , the rate of N_2 escape from inside the polymer interior is k_{esc} , the rate of N_2 diffusion into the bulk water is k_{diff} , and the rate of N_2 incorporation into a bubble is k_{bub} . Note that k_{photo} depends on light intensity and the molecule used, while the other rate constants should not vary. These equations can be solved analytically with the initial conditions $C_{N_2}^{in}(0) = C_{N_2}^{out}(0) = V_{bub}(0) = 0$. The solution is a rather long expression for the time dependent volume of N_2 contained in the bubbles:

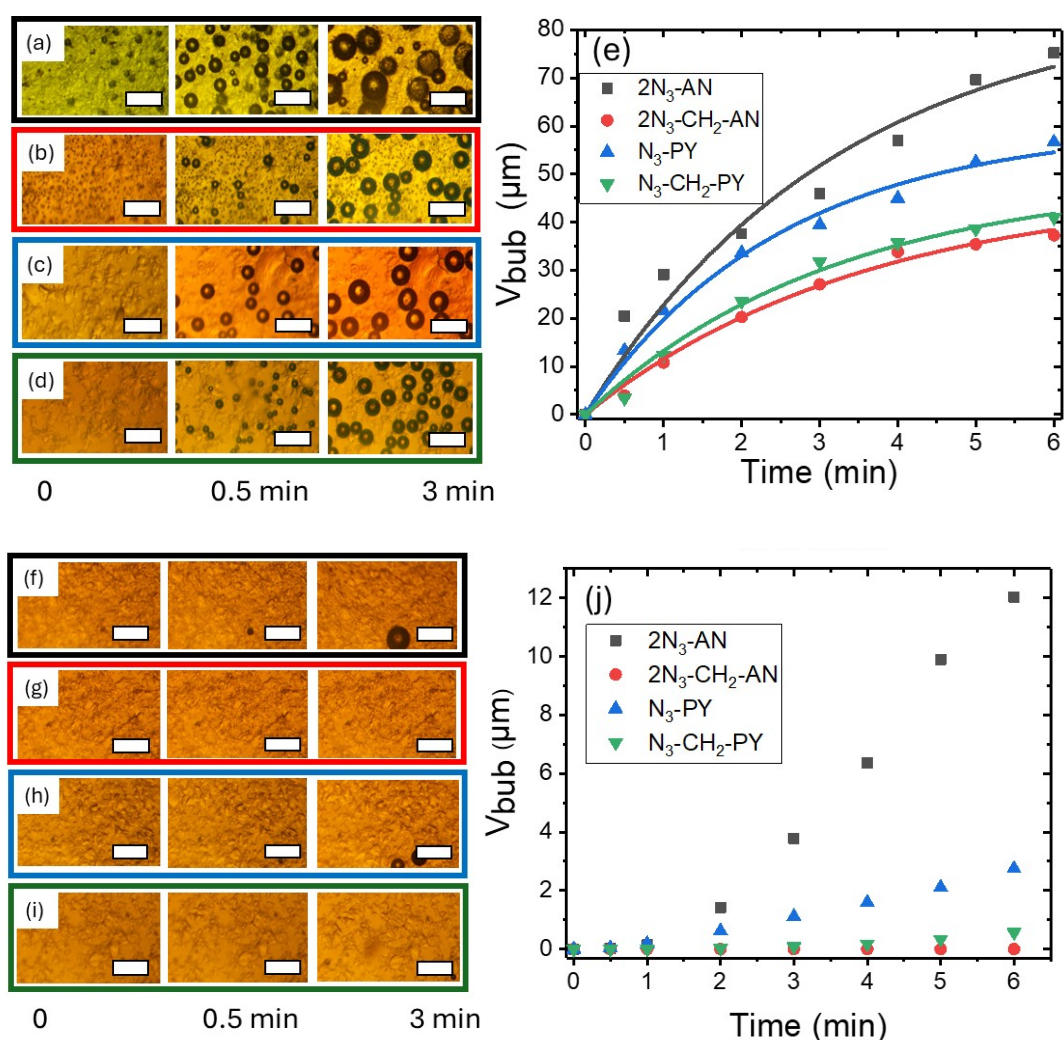


Figure 4. Images of bubble growth on PMMA surfaces with 0.1 M azide doping. Top: Films irradiated at 365 nm (10 mW/cm²) doped with (a) 2N₃-AN, (b) 2N₃-CH₂-AN, (c) N₃-PY (d) N₃-CH₂-PY. (e) The areal volume of bubbles $\bar{V}_{bub}(t)$ plotted versus time for the four azides. Bottom: Films irradiated at 365 nm (0.1 mW/cm²) doped with (f) 2N₃-AN, (g) 2N₃-CH₂-AN, (h) N₃-PY (i) N₃-CH₂-PY. (j) The areal volume of bubbles $\bar{V}_{bub}(t)$ plotted versus time for the four azides. Scale bars: 500 μm.

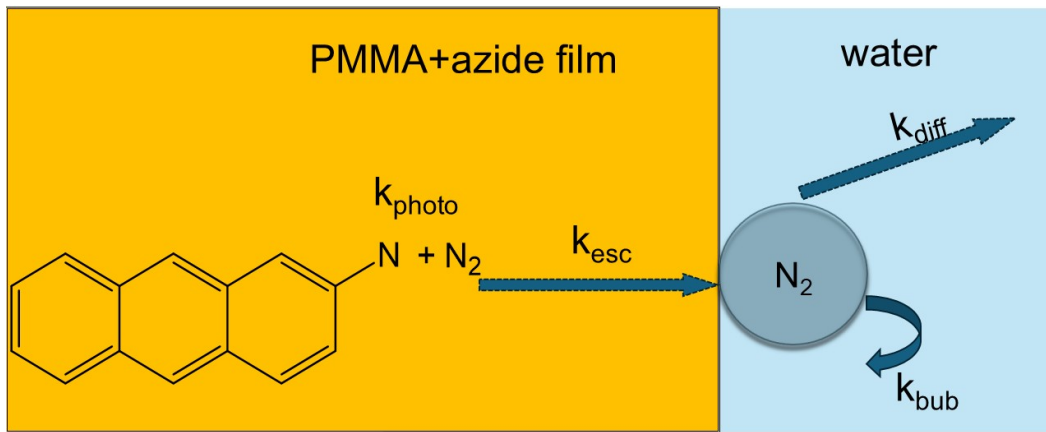


Figure 5. Schematic illustration of the kinetic processes and rates used for modeling the time-dependent growth of N_2 bubbles on the surface of the PMMA film.

$$\bar{V}_{bub}(t) = \frac{k_{bub}k_{esc}k_{photo}C_{azide}(0)}{k_{esc} - k_{photo}} \left(\frac{e^{-k_{esc}t}}{k_{esc}(k_{bub} - k_{diff} - k_{esc})} - \frac{e^{-k_{photo}t}}{k_{photo}(k_{bub} - k_{diff} - k_{photo})} \right) + C \quad (2)$$

$$C = \frac{k_{esc} - k_{photo}}{(k_{bub} - k_{diff})(k_{bub} - k_{diff} - k_{esc})(k_{bub} - k_{diff} - k_{photo})} + \frac{1}{k_{photo}(k_{bub} - k_{diff} - k_{photo})} - \frac{1}{k_{esc}(k_{bub} - k_{diff} - k_{esc})}$$

Equation (2) can be used to simulate the experimental $\bar{V}_{bub}(t)$ for $2N_3$ -AN under different light intensities. The simulated curves are overlaid with experimental data in Figure 6, and the kinetic parameters used to simulate the growth curves are summarized in Table 3. At high intensities, a large k_{photo} value means that the photolysis is not rate-limiting and the bubble growth is determined by the transport and nucleation rates. This is the situation for all the azides when $I = 10 \text{ mW/cm}^2$ and explains why they exhibit similar $\bar{V}_{bub}(t)$ curves at this intensity. As k_{photo} decreases, the photolysis rate eventually becomes the rate limiting step for bubble growth on the polymer surface. It is in this low intensity regime that differences in photolysis rates become reflected in the observed bubble growth rates, as observed in Figure 4j.

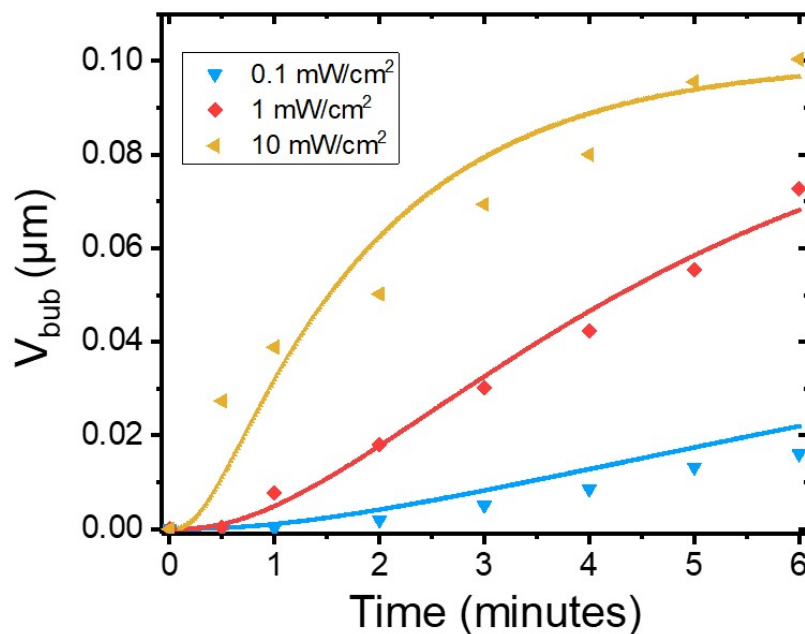


Figure 6. Experimental $\bar{V}_{bub}(t)$ curves measured for different 365 nm intensities for the 0.1 M $2N_3$ -AN/PMMA film (points) overlaid with fits (solid lines) using Equation (2) of the text and the parameters in Table 3.

Table 3. Kinetic parameters used to simulate the bubble growth curves in Figure 6 using Equation (2) in the text. The different values for k_{photo} correspond to the three different light intensities given in Figure 6.

Kinetic Parameter	Fit Values
Initial azide concentration	$C_{N_2(t)} = 0.1 \text{ M}$
Rate of azide photolysis	$k_{photo} = 0.01, 0.1, 1 \text{ s}^{-1}$
Rate of N_2 escape	$k_{esc} = 0.010 \text{ s}^{-1}$
Rate of bubble growth	$k_{bub} = 93 \times 10^{-3} \text{ s}^{-1}$
Rate of N_2 diffusion	$k_{diff} = 10 \times 10^{-11} \text{ s}^{-1}$

The important takeaway is that high light intensity can compensate for a low molecular reaction rate. At high intensities, all derivatives produced a dense layer of bubbles within a few minutes because the N_2 transport is rate-limiting and is similar for all azides. At lower intensities, however, the photolysis becomes rate-limiting, and the behavior of the different azides diverges. Under low-light conditions, $2N_3$ -AN will still form a dense bubble layer while $2N_3$ -CH₂-AN will generate almost no bubbles at all. While this multistep kinetic model captures the overall dynamics of N_2 bubble growth, it does not explicitly incorporate physical parameters like solvent hydrodynamics [35], bubble coalescence [36] and local gas depletion [37] that also influence bubble growth dynamics. These processes can be highly nonlinear and would be expected to cause the observed dynamics to deviate from first-order (linear) kinetics. Thus, the model presented here cannot be regarded as a first-principles description of the bubble formation, but rather as a framework for comparing kinetic trends across azide derivatives and light intensities.

In addition to the molecular photolysis rate, the multiple kinetic steps in our reaction scheme suggest that the polymer matrix should also play a key role in $\bar{V}_{bub}(t)$ by modifying k_{esc} . However, it does not appear that k_{esc} changes significantly in other polymer systems. We confirmed that azide photolysis could generate bubbles in other polymers besides PMMA. Rapid bubble growth was also observed for 0.1 M $2N_3$ -AN in both polystyrene and polycarbonate. At high intensities (10 mW/cm²) the growth rates and bubble volumes were within a factor of 2 of that in PMMA (Supplementary Figure S16, Supplementary Table S1), show that this strategy can be generalized to a variety of azide/polymer systems.

Sun et al. previously showed that nanoparticles doped with azides could generate N_2 bubbles via a photothermal mechanism. These bubbles could modulate ultrasound contrast in liquids [38,39]. We wanted to determine whether a surface layer of bubbles could generate useful contrast for an object imaged by a medical ultrasound device. PMMA is a biocompatible plastic that is extensively used in medical devices and implants [40]. The use of gas bubbles is now recognized as a safe and effective method to enhance contrast for biomedical ultrasound measurements [41–43]. In most ultrasound applications, the microbubbles are prepared ex situ as a particle containing gas enclosed in a shell composed of lipids, proteins, or polymer. The particle suspension is then injected into the biological medium or the organ to be imaged. Azide photolysis provides a method to generate N_2 bubbles in situ on surfaces, providing a way to generate bubbles on a specific object. Because it is a challenge to use ultrasound to image surgical instruments inside biological media [44], surface bubble generation could provide a complementary ultrasound imaging capability.

To mimic a surgical instrument, a glass pipette with a 2 mm diameter was coated with a layer of $2N_3$ -AN doped PMMA with a thickness of ~100 μm . When irradiated under water by an external 365 nm light source, the pipette tip rapidly developed a dense layer of bubbles, as shown in Figure 7a,c. This layer of bubbles increased the contrast when the pipette was imaged using a commercial ultrasound machine, as shown in Figure 7b,d. Using image analysis (Supplementary Figure S17), we found a 6 \times increase in image brightness after light exposure. This enhancement arises due to the large acoustic index mismatch at the liquid-gas interface [45], which is substantially larger than that of a liquid-solid interface. Moreover, the images in Figure 7 show that this effect leads to good visualization of the object sides, as well as the top surface. This proof-of-principle experiment demonstrates that light can be used to create a high density of bubbles that provides a useful contrast enhancement for medical ultrasound imaging.

One concern about using azide coatings in a biomedical setting is exposure to possibly toxic chemicals. Previously, we hypothesized that production of free N_2 inside the polymer creates an internal pressure that forces the N_2 molecules toward the surface [22]. This flow is several orders of magnitude larger than what would be expected based on random diffusion under equilibrium conditions [46,47]. If this is the case, then adding a second polymer layer to encapsulate the azide layer should still permit N_2 gas transport to the surface while alleviating concerns about possible toxicity of the azide component. To test this idea, we deposited a second layer of undoped PMMA on top of a layer doped with 0.1 M $2N_3$ -AN. Exposure of this bilayer sample to 365 nm light resulted in growth of a bubble layer with a slightly slower rate than that observed for the monolayer $2N_3$ -AN system

(Supplementary Figure S18). The ability of the photogenerated N_2 to flow through a neat PMMA capping layer shows that it is possible to avoid direct contact between the azide layer and the surrounding medium while still generating a layer of surface bubbles.

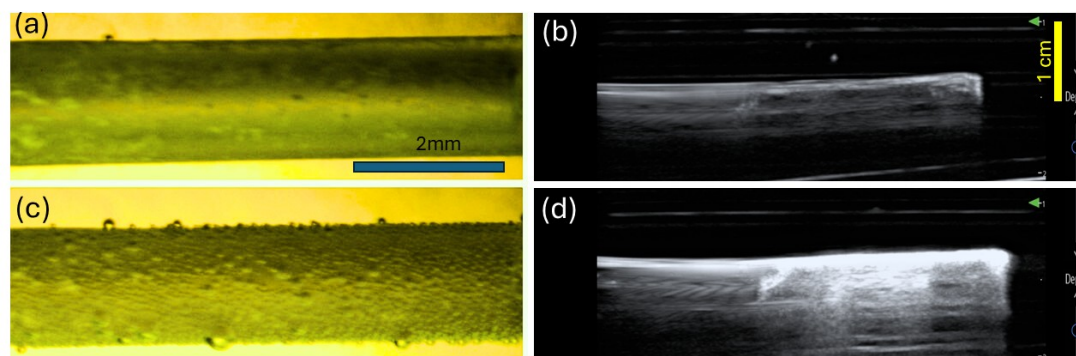


Figure 7. Photochemically generated bubbles enhance contrast in ultrasound imaging. A glass pipette tip is coated with a 0.1 M $2N_3$ -AN/PMMA film. (a) Optical and (b) ultrasound images before 365 nm irradiation. (c) Optical and (d) ultrasound images after irradiation, showing bubbles and enhanced ultrasound contrast.

4. Conclusions

The results in this paper demonstrate that the phenomenon of photochemical bubble generation can be extended to a variety of aromatic azide derivatives and biocompatible transparent polymers. While insertion of a methyl group between the aromatic absorber and reactive N_2 moiety decreased the photolysis rate, a multi-step first-order kinetic model was developed to show how lower molecular photolysis rates could be compensated for by higher light intensities. The bubble layer created by light exposure could significantly increase the contrast in a medical ultrasound imaging set-up. We also showed that the N_2 produced in the doped PMMA layer could be rapidly transported through a PMMA capping layer for surface bubble formation, so direct contact between the azide layer and the aqueous surroundings can be avoided. Taken together, the results here show that photochemical gas generation by solid polymer films is a general phenomenon that can be understood quantitatively and applied to ultrasound imaging. It is possible that future optimization of these photoactive polymer systems could lead to applications in medicine and other fields.

Supplementary Materials: The following supporting information can be downloaded at: <https://media.scilit.com/articles/others/2506271013537077/MI-983-Supplementary-Materials-v1.pdf>, Synthesis of compounds, UV Vis spectra, Bubble generation video on Polystyrene film, ultrasound imaging set-up. References [48–54] are cited in the Supplementary Materials.

Author Contributions: P.G. and C.B.: conceptualization, methodology, software, data curation, writing—original draft preparation, visualization, investigation; C.G.: Ultrasound imaging; Y.A. and M.A.: synthesis; R.K.: synthesis, writing—reviewing and editing. All authors have read and agreed to the published version of the manuscript”.

Funding: This work was supported by ONR under grant/contract N00014-24-1-2358 (C.J.B). The views expressed are those of the author and do not reflect the official policy or position of the Department of Defense or the U.S. Government. This work was also supported by the King Abdullah International Medical Research Center (KSAU-HS/KAIMRC) through grant NRC21R25003 (R.O.K.).

Data Availability Statement: Raw data will be made available upon reasonable request.

Conflicts of Interest: The authors declare no conflict of interest.

References

1. Hoffman, A.S. Stimuli-Responsive Polymers: Biomedical Applications and Challenges for Clinical Translation. *Adv. Drug Deliv. Rev.* **2013**, *65*, 10–16. <https://doi.org/10.1016/j.addr.2012.11.004>.
2. Wei, M.; Gao, Y.; Li, X.; Serpe, M.J. Stimuli-Responsive Polymers and Their Applications. *Polym. Chem.* **2017**, *8*, 127–143. <https://doi.org/10.1039/C6PY01585A>.
3. Zhao, Y.; Hua, M.; Yan, Y.; Wu, S.; Alsaid, Y.; He, X. Stimuli-Responsive Polymers for Soft Robotics. *Annu. Rev. Control Robot. Auton. Syst.* **2022**, *5*, 515–545. <https://doi.org/10.1146/annurev-control-042920-014327>.
4. McCormick, M.E.; Bhattacharyya, R. Drag Reduction of a Submersible Hull by Electrolysis. *Nav. Eng. J.* **1973**, *85*, 11–16. <https://doi.org/10.1111/j.1559-3584.1973.tb04788.x>.
5. Murai, Y. Frictional Drag Reduction by Bubble Injection. *Exp. Fluids* **2014**, *55*, 1773. <https://doi.org/10.1007/s00348-014-1773-x>.

6. Kim, H.; Chang, J.H. Increased Light Penetration Due to Ultrasound-Induced Air Bubbles in Optical Scattering Media. *Sci. Rep.* **2017**, *7*, 16105. <https://doi.org/10.1038/s41598-017-16444-9>.
7. Bhanawat, A.; Zhu, K.; Pilon, L. How Do Bubbles Affect Light Absorption in Photoelectrodes for Solar Water Splitting? *Sustain. Energy Fuels* **2022**, *6*, 910–924. <https://doi.org/10.1039/D1SE01730F>.
8. Domenico, S.N. Acoustic Wave Propagation in Air-bubble Curtains in Water—Part I: History and Theory. *Geophysics* **1982**, *47*, 345–353. <https://doi.org/10.1190/1.1441340>.
9. Leroy, V.; Strybulevych, A.; Lanoy, M.; Lemoult, F.; Tourin, A.; Page, J.H. Superabsorption of Acoustic Waves with Bubble Metascreens. *Phys. Rev. B* **2015**, *91*, 020301. <https://doi.org/10.1103/PhysRevB.91.020301>.
10. Sharma, G.S.; Skvortsov, A.; MacGillivray, I.; Kessissoglou, N. Sound Scattering by a Bubble Metasurface. *Phys. Rev. B* **2020**, *102*, 214308. <https://doi.org/10.1103/PhysRevB.102.214308>.
11. Huang, Z.; Zhao, S.; Su, M.; Yang, Q.; Li, Z.; Cai, Z.; Zhao, H.; Hu, X.; Zhou, H.; Li, F.; et al. Bioinspired Patterned Bubbles for Broad and Low-Frequency Acoustic Blocking. *ACS Appl. Mater. Interfaces* **2020**, *12*, 1757–1764. <https://doi.org/10.1021/acsami.9b15683>.
12. Gong, X.-T.; Zhou, H.-T.; Zhang, S.-C.; Wang, Y.-F.; Wang, Y.-S. Tunable Sound Transmission through Water–Air Interface by Membrane-Sealed Bubble Metasurface. *Appl. Phys. Lett.* **2023**, *123*, 231703. <https://doi.org/10.1063/5.0171461>.
13. Goyal, R.; Athanassiadis, A.G.; Ma, Z.; Fischer, P. Amplification of Acoustic Forces Using Microbubble Arrays Enables Manipulation of Centimeter-Scale Objects. *Phys. Rev. Lett.* **2022**, *128*, 254502. <https://doi.org/10.1103/PhysRevLett.128.254502>.
14. Liang, X.; Kumar, V.; Ahmadi, F.; Zhu, Y. Manipulation of Droplets and Bubbles for Thermal Applications. *Droplet* **2022**, *1*, 80–91. <https://doi.org/10.1002/dro2.21>.
15. Metwally, K.; Mensah, S.; Baffou, G. Fluence Threshold for Photothermal Bubble Generation Using Plasmonic Nanoparticles. *J. Phys. Chem. C* **2015**, *119*, 28586–28596. <https://doi.org/10.1021/acs.jpcc.5b09903>.
16. Baffou, G.; Polleux, J.; Rigneault, H.; Monneret, S. Super-Heating and Micro-Bubble Generation around Plasmonic Nanoparticles under Cw Illumination. *J. Phys. Chem. C* **2014**, *118*, 4890–4898. <https://doi.org/10.1021/jp411519k>.
17. Li, J.; Zhao, F.; Deng, Y.; Liu, D.; Chen, C.-H.; Shih, W.-C. Photothermal Generation of Programmable Microbubble Array on Nanoporous Gold Disks. *Opt. Express* **2018**, *26*, 16893. <https://doi.org/10.1364/OE.26.016893>.
18. Ohannesian, N.; Li, J.; Misbah, I.; Zhao, F.; Shih, W.-C. Directed Concentrating of Micro-/Nanoparticles via Near-Infrared Laser Generated Plasmonic Microbubbles. *ACS Omega* **2020**, *5*, 32481–32489. <https://doi.org/10.1021/acsomega.0c04610>.
19. Hu, M.; Wang, F.; Chen, L.; Huo, P.; Li, Y.; Gu, X.; Chong, K.L.; Deng, D. Near-Infrared-Laser-Navigated Dancing Bubble within Water via a Thermally Conductive Interface. *Nat. Commun.* **2022**, *13*, 5749. <https://doi.org/10.1038/s41467-022-33424-4>.
20. Prosperetti, A. Vapor Bubbles. *Annu. Rev. Fluid Mech.* **2017**, *49*, 221–248. <https://doi.org/10.1146/annurev-fluid-010816-060221>.
21. Shields, D.J.; Karothu, D.P.; Sambath, K.; Ranaweera, R.A.A.U.; Schramm, S.; Duncan, A.; Duncan, B.; Krause, J.A.; Gudmundsdottir, A.D.; Naumov, P. Cracking under Internal Pressure: Photodynamic Behavior of Vinyl Azide Crystals through N₂ Release. *J. Am. Chem. Soc.* **2020**, *142*, 18565–18575. <https://doi.org/10.1021/jacs.0c07830>.
22. Ghate, P.P.; Hanson, K.M.; Lam, K.; Al-Kaysi, R.O.; Bardeen, C.J. Generating Stable Nitrogen Bubble Layers on Poly(Methyl Methacrylate) Films by Photolysis of 2-Azidoanthracene. *Langmuir* **2024**, *40*, 4054–4062. <https://doi.org/10.1021/acs.langmuir.3c02869>.
23. Biswas, B.; Venkateswarulu, M.; Gaur, P.; Sharma, Y.; Sinha, S.; Ghosh, S. Triggered Emission for Rapid Detection of Hydrogen Sulfide Chaperoned by Large Stokes Shift. *J. Photochem. Photobiol. A Chem.* **2019**, *371*, 264–270. <https://doi.org/10.1016/j.jphotochem.2018.11.011>.
24. Pinchasik, B.-E.; Schönfeld, F.; Kappl, M.; Butt, H.-J. Bubbles Nucleating on Superhydrophobic Micropillar Arrays under Flow. *Soft Matter* **2019**, *15*, 8175–8183. <https://doi.org/10.1039/C9SM01224A>.
25. Deng, X.; Shan, Y.; Meng, X.; Yu, Z.; Lu, X.; Ma, Y.; Zhao, J.; Qiu, D.; Zhang, X.; Liu, Y.; et al. Direct Measuring of Single-Heterogeneous Bubble Nucleation Mediated by Surface Topology. *Proc. Natl. Acad. Sci. USA* **2022**, *119*, e2205827119. <https://doi.org/10.1073/pnas.2205827119>.
26. Beechem, J.M.; Ameloot, M.; Brand, L. Global and Target Analysis of Complex Decay Phenomena. *Instrum. Sci. Technol.* **1985**, *14*, 379–402. <https://doi.org/10.1080/10739148508543585>.
27. Reiser, A.; Bowes, G.; Horne, R.J. Photolysis of Aromatic Azides. Part 1—Electronic Spectra of Aromatic Nitrenes and Their Parent Azides. *Trans. Faraday Soc.* **1966**, *62*, 3162–3169. <https://doi.org/10.1039/TF9666203162>.
28. Alvarado, R.; Grivet, J.-P.; Igier, C.; Barcelo, J.; Rigaudy, J. Spectroscopic Studies of Azides and Nitrenes Derived from Anthracene. *J. Chem. Soc., Faraday Trans.* **1977**, *73*, 844. <https://doi.org/10.1039/f29777300844>.
29. Wentrup, C. Nitrenes, Carbenes, Diradicals, and Ylides. Interconversions of Reactive Intermediates. *Acc. Chem. Res.* **2011**, *44*, 393–404. <https://doi.org/10.1021/ar700198z>.

30. Sankaranarayanan, J.; Rajam, S.; Hadad, C.M.; Gudmundsdottir, A.D. The Ability of Triplet Nitrenes to Abstract Hydrogen Atoms. *J Phys. Org. Chem.* **2010**, *23*, 370–375. <https://doi.org/10.1002/poc.1654>.
31. Reiser, A.; Marley, R. Photolysis of Aromatic Azides. Part 3—Quantum Yield and Mechanism. *Trans. Faraday Soc.* **1968**, *64*, 1806–1815. <https://doi.org/10.1039/TF9686401806>.
32. Gritsan, N.P.; Pritchina, E.A. The Mechanism of Photolysis of Aromatic Azides. *Russ. Chem. Rev.* **1992**, *61*, 500–516. <https://doi.org/10.1070/RC1992v061n05ABEH000959>.
33. Soto, J.; Otero, J.C. Conservation of El-Sayed's Rules in the Photolysis of Phenyl Azide: Two Independent Decomposition Doorways for Alternate Direct Formation of Triplet and Singlet Phenylnitrene. *J. Phys. Chem. A* **2019**, *123*, 9053–9060. <https://doi.org/10.1021/acs.jpca.9b06915>.
34. Rubin, M.B.; Noyes, R.M. Thresholds for Nucleation of Bubbles of Nitrogen in Various Solvents. *J. Phys. Chem.* **1992**, *96*, 993–1000. <https://doi.org/10.1021/j100181a082>.
35. Maloth, R.K.N.; Khayat, R.E.; DeGroot, C.T. Bubble Growth in Supersaturated Liquids. *Fluids* **2022**, *7*, 365. <https://doi.org/10.3390/fluids7120365>.
36. Huber, C.; Su, Y.; Nguyen, C.T.; Parmigiani, A.; Gonnermann, H.M.; Dufek, J. A New Bubble Dynamics Model to Study Bubble Growth, Deformation, and Coalescence. *JGR Solid Earth* **2014**, *119*, 216–239. <https://doi.org/10.1002/2013JB010419>.
37. Moreno Soto, Á.; Prosperetti, A.; Lohse, D.; Van Der Meer, D. Gas Depletion through Single Gas Bubble Diffusive Growth and Its Effect on Subsequent Bubbles. *J. Fluid Mech.* **2017**, *831*, 474–490. <https://doi.org/10.1017/jfm.2017.623>.
38. Sun, I.-C.; Emelianov, S. Gas-Generating Nanoparticles for Contrast-Enhanced Ultrasound Imaging. *Nanoscale* **2019**, *11*, 16235–16240. <https://doi.org/10.1039/C9NR04471J>.
39. Sun, I.-C.; Dumani, D.S.; Emelianov, S.Y. Applications of the Photocatalytic and Photoacoustic Properties of Gold Nanorods in Contrast-Enhanced Ultrasound and Photoacoustic Imaging. *ACS Nano* **2024**, *18*, 3575–3582. <https://doi.org/10.1021/acsnano.3c11223>.
40. Frazer, R.Q.; Byron, R.T.; Osborne, P.B.; West, K.P. PMMA: An Essential Material in Medicine and Dentistry. *J. Long Term Eff. Med. Implant.* **2005**, *15*, 629–639. <https://doi.org/10.1615/JLongTermEffMedImplants.v15.i6.60>.
41. Blomley, M.J.K. Science, Medicine, and the Future: Microbubble Contrast Agents: A New Era in Ultrasound. *BMJ* **2001**, *322*, 1222–1225. <https://doi.org/10.1136/bmj.322.7296.1222>.
42. Lee, H.; Kim, H.; Han, H.; Lee, M.; Lee, S.; Yoo, H.; Chang, J.H.; Kim, H. Microbubbles Used for Contrast Enhanced Ultrasound and Theragnosis: A Review of Principles to Applications. *Biomed. Eng. Lett.* **2017**, *7*, 59–69. <https://doi.org/10.1007/s13534-017-0016-5>.
43. Ferrara, K.; Pollard, R.; Borden, M. Ultrasound Microbubble Contrast Agents: Fundamentals and Application to Gene and Drug Delivery. *Annu. Rev. Biomed. Eng.* **2007**, *9*, 415–447. <https://doi.org/10.1146/annurev.bioeng.8.061505.095852>.
44. Huang, J.; Triedman, J.K.; Vasilyev, N.V.; Suematsu, Y.; Cleveland, R.O.; Dupont, P.E. Imaging Artifacts of Medical Instruments in Ultrasound-Guided Interventions. *J. Ultrasound Med.* **2007**, *26*, 1303–1322. <https://doi.org/10.7863/jum.2007.26.10.1303>.
45. Godin, O.A. Sound Transmission through Water–Air Interfaces: New Insights into an Old Problem. *Contemp. Phys.* **2008**, *49*, 105–123. <https://doi.org/10.1080/00107510802090415>.
46. Patel, V.M.; Patel, C.K.; Patel, K.C.; Patel, R.D. Diffusion of Gases in Poly(Methyl Methacrylate). *Makromol. Chem.* **1972**, *158*, 65–79. <https://doi.org/10.1002/macp.1972.021580107>.
47. Haraya, K.; Hwang, S.-T. Permeation of Oxygen, Argon and Nitrogen through Polymer Membranes. *J. Membr. Sci.* **1992**, *71*, 13–27. [https://doi.org/10.1016/0376-7388\(92\)85002-Z](https://doi.org/10.1016/0376-7388(92)85002-Z).
48. Kung, Y.-C.; Hsiao, S.-H. Fluorescent and Electrochromic Polyamides with Pyrenylamine Chromophore. *J. Mater. Chem.* **2010**, *20*, 5481.
49. Bräse, S.; Banert, K., Eds.; *Organic Azides: Syntheses and Applications*; John Wiley: Chichester, UK, 2010.
50. Morales-Espinoza, E.G.; Lijanová, I.V.; Morales-Saavedra, O.G.; Torres-Zuñiga, V.; Hernandez-Ortega, S.; Martínez-García, M. Synthesis of Porphyrin-Dendrimers with a Pyrene in the Periphery and Their Cubic Nonlinear Optical Properties. *Molecules* **2011**, *16*, 6950–6968.
51. Ingale, S.A.; Seela, F. A Ratiometric Fluorescent On–Off Zn²⁺ Chemosensor Based on a Tripropargylamine Pyrene Azide Click Adduct. *J. Org. Chem.* **2012**, *77*, 9352–9356.
52. Jiang, J.; Lima, O.V.; Pei, Y.; Jiang, Z.; Chen, Z.; Yu, C.; Wang, J.; Zeng, X.C.; Forsythe, E.; Tan, L. Self-Assembled Nanolayers of Conjugated Silane with π – π Interlocking. *ACS Nano* **2010**, *4*, 3773–3780.
53. Okita, T.; Muto, K.; Yamaguchi, J. Decarbonylative Methylation of Aromatic Esters by a Nickel Catalyst. *Org. Lett.* **2018**, *20*, 3132–3135.
54. Arjunan, P.; Berlin, K.D. An improved synthesis of 2-anthraldehyde. *Org. Prep. Proced. Int.* **1981**, *13*, 368–371.